CHARACTERIZATION OF TUBULAR CHRYSOTILE BY THERMOPOROMETRY, NITROGEN SORPTION, DRIFTS, AND TEM*

MARK K. TITULAER,[1] J. CEES VAN MILTENBURG,[2] J. BEN H. JANSEN,[1] AND JOHN W. GEUS[3]

[1] Department of Geochemistry, Institute for Earth Sciences
University of Utrecht, Budapestlaan 4, P.O. Box 80.021
3508 TA Utrecht, The Netherlands

[2] Chemical Thermodynamics Group, University of Utrecht, Transitorium 3
Padualaan 8, 3584 CH Utrecht, The Netherlands

[3] Department of Inorganic Chemistry, University of Utrecht, Sorbonnelaan 16
P.O. Box 80.083, 3508 TB Utrecht, The Netherlands

Abstract—The maximum crystal radius R_n of ice in hollow wet chrysotile tubes is established by thermoporometry to be between 2.8 and 3.2 nm, and the internal pore volume V_n of the tubes to be between 0.008 and 0.02 ml/g. The hollow tubes of chrysotile and, for comparative reasons, small plates of talc, are hydrothermally synthesized at temperatures between 563 and 600 K and at pressures between 75 and 120 hPa. Size and shape of the pores can be varied by changing the Mg/Si molar ratios in steps of 3/1.5 and 3/2 for chrysotile and 3/3.6 and 3/4 for talc. The tubular morphology of the aggregates dried at 393 K is investigated by 1) transmission electron microscopy (TEM), 2) nitrogen adsorption and desorption at 77 K, and 3) diffuse reflectance infrared fourier transformed spectroscopy (DRIFTS). The radius within the hollow tubes, R_i, is between 2.5 and 4.0 nm as measured by TEM, and between 2.8 and 3.2 nm as determined by nitrogen adsorption and desorption. The measured radii agree well with the value calculated from crystallographic data, which is smaller than 5.3 nm. Within the dried aggregates the tubes are clustered in regular patterns, in which each tube is surrounded by six other tubes. The external radius, R_o, between the clustered tubes is from 1.6 to 2.9 nm as observed by TEM, and from 1.8 to 2.3 nm by N_2 adsorption and desorption. The external radius is not measured by thermoporometry. Where thermoporometry only measures the average pore size and pore volume within the tubes, TEM and N_2 adsorption and desorption additionally provide the corresponding values between the tubes. A third pore radius, 5 to 20 nm between the clusters of chrysotile tubes, is established with N_2 adsorption and desorption.

Key Words—Chrysotile asbestos, Infrared spectroscopy, N_2 adsorption and desorption, Thermoporometry, Transmission electron microscopy, X-ray diffraction.

INTRODUCTION

Theoretical background

In many studies the freezing point depression of water in soils and clays is investigated in combination with effects such as frost-heaving, frost-damage, and an amount of non-freezing water. The fact that various processes can affect formation of ice in soils and clays is known only to a few scientists. One technique that can monitor the formation of ice-nuclei in porous materials is thermoporometry. After a short theoretical background of thermoporometry, the processes that take place with thermoporometry are compared with those accompanied with frost-heaving, frost-damage, and distillation of pore water to large ice-crystals outside the pores of the solid. Thermoporometry yields information about the pore size, pore volume, and the pore shape of porous materials in water and is based on the depression of the solidification point of a fluid, such as water, benzene, and dicyclohexane ($C_{10}H_{18}$)

(Higuti and Iwagami, 1952; Jallut *et al.*, 1992; Jackson and McKenna, 1992; Titulaer, 1993). Water has the advantage over benzene in the determination of the pore size, in that the solid does not have to be dried first, which may cause a decrease of the pore volume. In the case of water, thermodynamics predict the formation of ice within narrow pores at temperatures lower than the freezing point of bulk water, i.e., T_o at 273.15 K. Provided the concentration of soluble salts within the pores of the solid is negligible, the freezing point depression, dT_s, which is $T–T_o < 0$, is a function of the pore radius. Thermoporometry has been applied to characterize wet silica gels (Jallut *et al.*, 1992; Higuti and Iwagami, 1952) and, recently, polymers (Cuperus *et al.*, 1992; Sasthav *et al.*, 1992). Jallut *et al.* (1992) have published a state-of-the-art critical review.

The amount of water freezing or melting within the porous system can be detected separately from the bulk water by differential scanning calorimetry (DSC). The heat-flow accompanied with freezing of water or thawing of ice within the porous solid is recorded as a function of the temperature in a linear temperature program. Thermoporometry enables one to measure ice

---

496
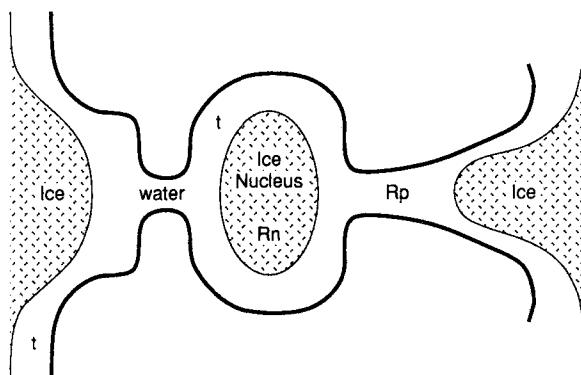
Figure 1. Formation of a critical ice-nucleus with radius R_n, and the penetration of the ice-meniscus in the solid.
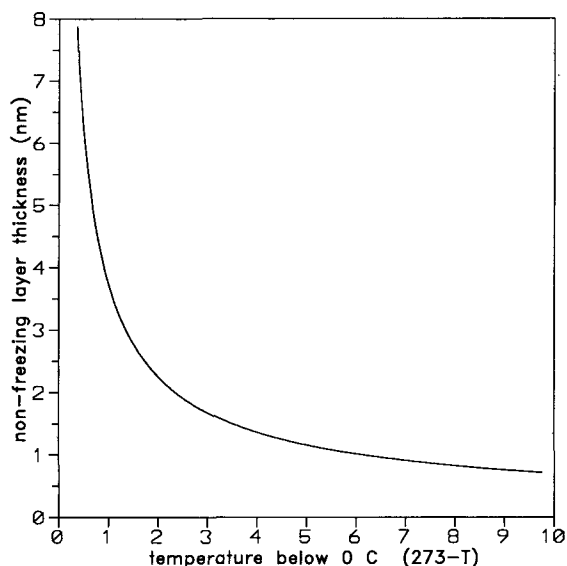

Figure 2. Measured relationship between the average statistical thickness of the layer of unfrozen water and the temperature below 0°C for the minerals kaolinite, basalt, and limonite-goethite (Banin and Anderson, 1971).

crystal radii, R_n, between 1 and 150 nm (Quinson *et al.*, 1987). The minimum value of 1 nm of the radius, R_n, that can be measured is due to 1) the minimum temperature of 210 K that can be established within the DSC apparatus used in this work with gaseous nitrogen as a cooling agent and 2) the fact that water present in pores of radii, R_p, smaller than approximately 1 nm or interlayer distances smaller than 2 nm is strongly bonded to the surface of the pore and does not freeze (Ehrburger *et al.*, 1985). Interference with the peaks of 'bulk water' and 'pore water' in the thermogram leads to the upper limit of 150 nm.

Thermoporometry is based upon the fact that the temperature at which a liquid freezes or melts depends upon the curvature of the interface between the liquid and the solid. The freezing temperature is a function of the pore radius, R_p, within the solid on the condition that the pores are completely filled with water. Ice will form a continuous plastic mass in the pores and freezing proceeds by 1) migration of the ice-water interface into the porous material (Sasthav *et al.*, 1992) or 2) nucleation of the solid within the pores of the material provided the radius of the smallest stable nucleus fits in the pore (Figure 1). The radius of the ice-nucleus, R_n (nm), is a function of the freezing point depression, $dT_s = T_s - 273.15$, by:

$$R_n = -2\gamma_{ls} \cdot V_L / (dS_f^o \cdot dT_s) \quad (nm) \qquad (1)$$

where γ_{ls} is the ice-water surface tension (N/m), V_L the specific volume of water (m³/g), and dS_f^o the entropy of fusion (J/g·K); or:

$$R_n = -64.67/dT_s - 0.23 \quad (nm) \qquad (2)$$

where -64.67 is a constant in nm·K (Quinson *et al.*, 1987). Eq. (1) is alternatively formulated by Enüstün *et al.* (1990) by:

$$dT_s = -2\gamma_{ls} \cdot T_o / (D \cdot H_o \cdot R_n) \quad (K) \qquad (3)$$

where D is the density of water $(=1/V_L)$ and H_o the heat of fusion per unit mass $(H_o = dS_f^o \cdot T_o)$. As displayed in Figure 1 during penetration of the interface

into a porous material, the interface has to assume a semispherical shape of a radius that is equal to the radius of the pore minus a non-freezing layer of a thickness, t: $R_n = R_p - t$. The thickness, t, of the non-freezing layer of water between the ice crystal and the porous solid is a function of the freezing temperature as determined by Banin and Anderson (1971). The thickness, t, of the layer on mineral surfaces such as, kaolinite, basalt, and limonite-goethite is measured by the ratio of the volume of non-freezing water to the surface area of the solids. The thickness is reciprocal with the freezing point depression, dT_s, by:

$$t = -5/dT_s \quad (nm) \qquad (4)$$

The thickness, t, as a function of the freezing point depression is displayed in Figure 2. Since both the size of the non-freezing layer, t, and the ice-crystal radius, R_n, increase reciprocally with decrease in the freezing point depression, dT_s (Eqs. (1) and (4)), the size of the non-freezing layer is expected to increase linearly with the ice-crystal radius, R_n. Indeed, van der Grift *et al.* (1990) have observed a linearly increase of the non-freezing layer thickness, t, with increasing ice-crystal radius, R_n.

The non-freezing layer thickness decreases to 1 nm at a freezing point depression of -5 K. Below freezing point depressions of -5 K, the thickness of the unfrozen water layer lies in the range of 0.5–0.8 nm for almost every mineral. At these temperatures, the existence of the non-freezing layer of approximately three monolayers of water (Yazynina *et al.*, 1987) has been satisfactorily demonstrated by proton-NMR spectroscopy (Ehrburger *et al.*, 1985), DSC (Sakomoto *et al.*,
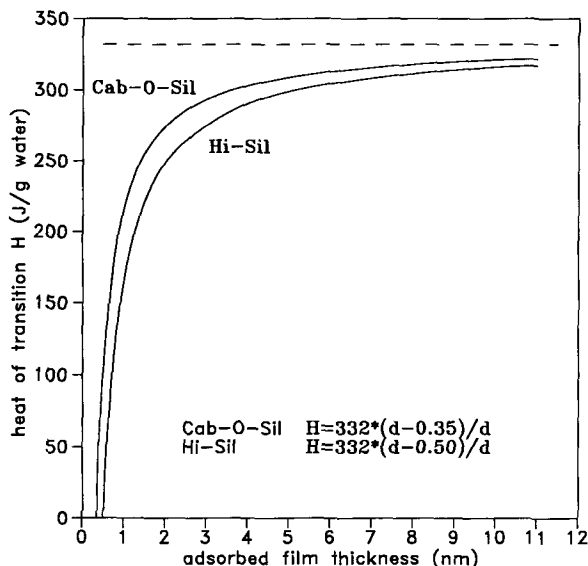
Figure 3. Heat of transition for water adsorbed on Cab-O-Sil and Hi-Sil *vs.* adsorbed film thickness, d (Plooster and Gitlin, 1971).

1989; Tasaka *et al.,* 1988), and viscosity measurements (Dedyulya and Churaev, 1988). An interesting study of the effect of the strongly adsorbed water layer comprising the non-freezing layer on the ice-water transformation energy, H, is made by Plooster and Gitlin (1971). The ice-water phase transition energy is determined for water adsorbed on pyrogenic Cab-O-Sil (surface area 190 m²/g) and precipitated Hi-Sil (133 m²/g) silica surfaces. They have plotted the heat of the ice-water transition energy, H, as a function of the adsorbed water film thickness, d, as displayed in Figure 3. It is assumed that the water forms a concentric spherical shell of unit density around each silica particle. The ice-water transformation energy lies below the value of bulk ice, H_o, of 332 J/g (dashed line in Figure 3), until the adsorbed water film thickness, d, is large. Plooster and Gitlin assume a continuous effect of the surface silanol groups forming multiple hydrogen bonds with the first layer of water. The first layer of adsorbed water will less strongly influence the structure of the next layer. Plooster and Gitlin (1971) assume the influence persists to a considerable distance from the surface. The specific enthalpy is assumed to increase, approaching the bulk value, with increasing distance from the particle surface. However, an unnoticed result of the findings in Plooster and Gitlin (1971) is the fact that the adsorbed water film can alternatively be split in a non-freezing layer with thickness, t, not undergoing the phase transformation and a layer of thickness, d-t, with merely the properties of bulk water. Their results can be fit with the relation H = H_o·(d-t)/d = 332·(d-t)/d, resulting in a non-freezing layer thickness, t, of 0.35 nm for more hydrophobous pyrogenic Cab-O-Sil

silica and 0.50 nm for more hydrophilous precipitated Hi-Sil-233 silica.

Transport of water or ice with freezing

The formation of an ice nucleus or penetration of the ice-meniscus into the porous solid as shown in Figure 1 occurs at a higher Gibbs energy than the formation of bulk ice outside the pores of the solid. Transport of ice or water from the micropores to large ice-crystals freezing outside the pores is likely to occur. There are three different processes that can occur with freezing of water: 1) the increased Gibbs free energy results in a large capillary pressure of ice formed in the pores of a few nms (Everett, 1961; Miller, 1973; Scherer, 1993); 2) volume expansion of ice formed with freezing of water in small pores, with ice-crystal radii $R_n \geq 2$ nm (Enüstün *et al.,* 1990); or 3) migration of unfrozen water in very small pores to large ice-lenses formed outside the pores. The pore radii, R_p, of these pores are as small as the non-freezing layer thickness of approximately 1 nm, or the interlayer distances in clays are as small as 2 nm (Ahlrich and White, 1962; Anderson and Hoekstra, 1965; Low *et al.,* 1968).

Everett (1961) has extensively dealt with the first mentioned process and the effect on the destruction of the solid (frost-damage) or the lifting of soil (frost-heaving). Everett (1961) and Miller (1973) emphasize that the destruction does not involve the second mentioned process. Additionally, liquids that occupy a lower volume with the transition to the solid can bring about disintegration due to transport of the solid to larger pores. The transport is due to the pressure gradient between pore and bulk ice, caused by the increased pressure of the ice-water meniscus in the porous material. The increased pressure of the ice-water meniscus is given by the Laplace equation:

$$P_{ice} - P_{water} = 2\gamma_{ls}/R_n \quad (Pa) \quad (5)$$

which, in combination with Eq. (1), results in:

$$P_{ice} - P_{water} = -dS_f^o \cdot dT_s/V_L \quad (Pa) \quad (6)$$

where $P_{ice} > P_{water}$, because $dT_s < 0$. Cracking of pores seems to proceed within the wide pores that are in contact with the narrow pores. Frost-damage is usually observed in soils with broad pore size distributions, small submicrometer pores in contact with large pores. Ice is extruded by the increased pressure of ice from the narrow pores into the wide pores that are cracked. Extrusion of ice is only expected if the ice meniscus is in direct contact with the bulk ice. If an isolated nucleus is formed in the pore as seen in Figure 1, the bulk ice cannot experience the increased pressure of the ice nucleus. Furthermore extrusion of ice requires the transport of water through the highly fixed non-freezing layer of about 1 nm into the pores. Since the external water outside the porous body is frozen first and forms a crystalline crust around the body, there is little water

available to replace the extruded ice in the pores, which reduces the pressure of water, P_{water}, and decreases the rate of extrusion. Clearly the extrusion occurs at a relatively low rate and doesn't seem to proceed within the thermoporometric measurement time. Titulaer (1993) observed that thermoporometry is a gentle non-destructive technique, able to measure ice-crystal radii, R_n, as small as 1.5–3.5 nm.

The second process of volume expansion of water with freezing permits the measurement of pore size distributions with a dilatometric technique, phase transition porometry (PTP). The technique is again appropriate to measure ice-crystal radii with $R_n \geq 2$ nm.

The third process involves distillation of pore water to large ice-crystals growing outside the pores. The process, which is due to the non-freezing layer of water in very small pores, is especially observed with expanded clays with interlayer spacings of 2 nm. The interlayer spacing decreases with freezing because of transport of water to the ice lenses formed between the clay particles (Alrich and White, 1962). The interlayer spacing of calcium-bentonite clay decreases from 1.0 to 0.6 nm by transport of water, while that of sodium-bentonite decreases from 2.3 to 0.9 nm, leaving only three layers of water in the interlayer (Anderson and Hoekstra, 1965).

Pore volume measurements by thermoporometry

The pore volume of the solid, V_n, expressed as the volume of ice in ml divided by the weight of the porous solid in g, is calculated by the summation of the heat-fluxes measured during freezing as a function of the temperature (Eq. (7));

$$V_n = \Sigma_i P_i \cdot (T_{i+1} - T_i)/(D \cdot H_o \cdot W \cdot sr) \quad (ml/g) \quad (7)$$

where P_i is the heat-flux in J/s measured at temperature T_i within the temperature interval $(T_{i+1} - T_i)$ of 0.04 K on the DSC, D is the density of ice, approximately 1 g/ml, H_o the solidification enthalpy of ice of about 332 J/g, W the weight of the porous material in g, and sr the scan rate of 0.5 K/min.

Since the presence of a non-freezing layer reduces the amount of ice that can be formed in the pore (Figure 1), the pore volume obtained by thermoporometry based on measuring the volume of the ice-crystal is expected to be lower than the real pore volume that includes the volume of the non-freezing layer. In Figure 4 it appears that the pore volume, V_n, determined thermoporometrically in silica gels, is consistently 0.2–0.3 ml/g lower than the volumes measured by mercury penetration and nitrogen sorption (Titulaer, 1993). The lower value measured by thermoporometry can be attributed to the non-freezing layer. At freezing point depression temperatures below −5 K, Titulaer (1993) could satisfactorily correct the ice volume and surface area to the pore volume and surface area as determined by nitrogen sorption with a value of the non-freezing
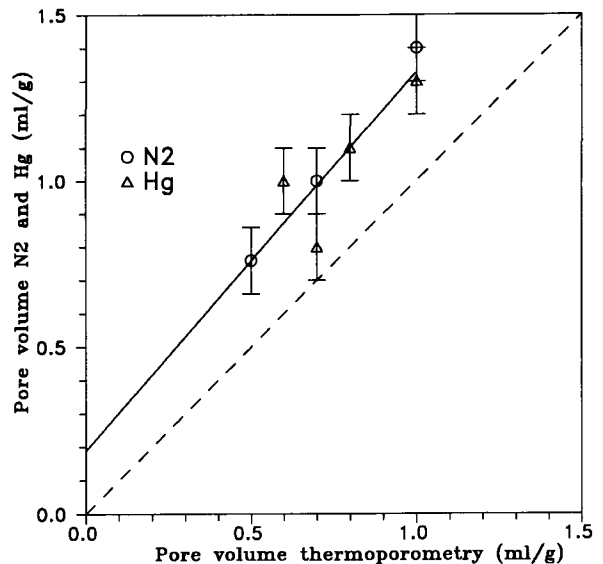

Figure 4. The pore volume, V_p, of nitrogen sorption and mercury penetration plotted against the ice pore volume, V_n, obtained by thermoporometry (Titulaer, 1993). The solid line represents the best fit of the data, while the dashed line assumes an equal pore volume of nitrogen sorption and thermoporometry.

layer of 0.9 nm. The value of 0.9 nm consisting of three monolayers of water is the average value mentioned in the literature (Brun *et al.*, 1978; Ehrburger *et al.*, 1985; Hench and West, 1990; Takagi, 1990).

Freezing and thawing hysteresis, the shape factor F

A considerable hysteresis takes place in the freezing point depression during the cooling step, dT_s, and the depression of the thawing temperature, dT_f, during the heating step of the measurement cycles. The freezing of pore water occurs at a considerably lower temperature than the thawing of pore ice and, consequently, $|dT_s| > |dT_f|$. The value $R_{heating}$, the size of the radius obtained in a heating experiment, is therefore larger than the $R_{cooling}$ measured in a cooling experiment (Eq. (7). The value of $R_{heating}/R_{cooling}$ is dependent on the pore shape. A pore shape determining factor F is introduced, which is expressed by Eq. (8). The theoretical value of F varies between 1 and 2, with a spherical and a cylindrical pore shape, respectively (Quinson *et al.*, 1987):

$$F = R_{heating}/R_{cooling}$$

$$= (64.67/dT_f - 0.23)/(64.67/dT_s - 0.23)$$

$$\approx dT_s/dT_f \quad (8)$$

where dT_s is the freezing point depression in the cooling step of the measuring sequence, and dT_f the melting point depression of the ice occupying the pores in the heating step. Freezing always occurs as a spherical nucleus or a semispherical penetrating meniscus; thus,
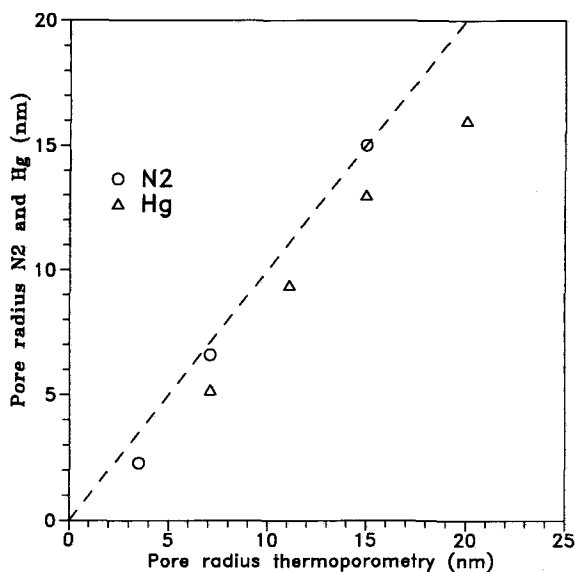
Figure 5. Pore radii, R_p, of silica gels by nitrogen sorption and mercury penetration plotted against the radii, R_n, obtained by thermoporometry (Titulaer, 1993).

$$R_{body} - t = R_n \approx R_{neck} \quad (nm) \qquad (9)$$

Additionally Titulaer (1993) shows that isolated ice-nuclei in ink-bottle-shaped pores can be formed. In Figure 5, the mean pore radii in silica gels as determined by mercury porosimetry and nitrogen desorption are plotted as a function of the pore radius resulting from thermoporometry. Though the agreement is remarkably good, the values determined thermoporometrically being equal or even larger than those measured by mercury penetration and nitrogen desorption are unexpected. The presence of the non-freezing layer of water suggests the pore radii determined by thermoporometry should be smaller than those measured by nitrogen desorption or mercury intrusion. With ink-bottle pores, however, desorption of nitrogen and penetration of mercury is dominated by the relatively small entrance of the pores. With thermoporometry the radius of the spherical pore itself and not that of the entrance is measured (Figure 1).

Chrysotile fibers, belonging to the serpentine mineral group, with the formula $Mg_3Si_2O_5(OH)_4$ display a perfectly cylindrical pore shape (Noll and Kircher, 1951; Noll *et al.*, 1958). The pore shape is of interest to check the theoretical assumptions of the thermoporometric characterization, e.g., the pore shape factor, F, and the non-freezing layer, t. Earlier, Scholten *et al.* (1975) used chrysotile tubes to check the validity of the Kelvin equation for capillary condensation of N_2 at 77 K, and the Washburn equation for penetration of mercury into the tubes. In this work, thermoporometry is applied to fibrous chrysotile, and for comparative reasons also to talc platelets, of the formula $Mg_3Si_4O_{10}(OH)_2$.

$dT_s \sim 1/R_1 + 1/R_2 = 2/R_n$, where R_1 and R_2 are the radii of curvature of the ice-sphere ($R_1 = R_2 = R_n$). With thawing, however, it is assumed that pore ice has the shape of the pore ($R_1 \neq R_2$) and melts from the pore wall at a rate governed by the radii of curvature of the pore wall, thus resulting for a cylindrical pore in a thawing point depression $dT_f \sim 1/R_1 + 1/\infty = 1/R_n$ ($R_1 = R_n$, $R_2 = \infty$) and a shape factor of 2. In a purely spherical pocket, the ice-crystal remains spherical and $dT_f \sim 1/R_1 + 1/R_2 = 2/R_n$; the thawing temperature is at the same temperature as the freezing temperature; and the shape factor is 1. The hysteresis is, therefore, explained by the non-spherical shape of the pores.

Enüstün *et al.* (1990) explain the hysteresis of the freezing and thawing temperature differently. In the opinion of Enüstün *et al.* (1990) and Scherer (1993) the isolated ice-nucleus cannot be formed, and only the penetration of the semispherical ice-meniscus takes place (Figure 1). Consequently, with ink-bottle-shaped pores the $R_{cooling}$ is governed by the relatively small neck of the pore, and $R_{neck} = R_{cooling}$. The thawing occurs in the relatively large body of the pore and $R_{body} = R_{heating}$. Since the body radius, R_{body}, is larger than the neck radius, R_{neck}, the freezing point depression $|dT_s|$ is considerably larger than the thawing point depression, $|dT_f|$, and the thawing occurs at a higher temperature. The radius, R_n, in a cooling experiment agreed well with the radius of the neck determined with electron microscopy. However, a weak point in their model is the fact that they entirely neglect the presence of the non-freezing layer. Especially in small ink-bottle-shaped pores, the body radius minus the non-freezing layer thickness might be equal to the neck radius:

Structure of chrysotile

The curvature of the tubes is due to the structure of the individual unit cells of clinochrysotile. Figure 6 shows the projection of the monoclinic unit cell of clinochrysotile ($Mg_3Si_2O_5(OH)_4$) in the ab plane. The space group of clinochrysotile is C_m (Deer *et al.*, 1962). The oxygens of the SiO_4 tetrahedra not involved in the siloxane bonds point upwards and are connected to the brucite sheet. The brucite sheet contains Mg octahedrally coordinated to oxygen, four of which are from OH groups.

Noll and Kircher (1951) and Noll *et al.* (1958) previously studied the curvature in the b-direction of the layers. Without the curvature, a considerable misfit exists between the silica and brucite sheets as illustrated by the differences of the sheet parameters. A calculation in the b-direction is usually performed.

The brucite sheet exhibits lengths of $a_b = 0.54$ and $b_b = 0.94$ nm ($b_b = \sqrt{3a_b}$), and the silica sheet $a_s = 0.50$ and $b_s = 0.87$ nm (Noll and Kircher, 1951). A bending in the b-direction partly relieves the stress between the two sheets, the smaller silica sheet being on the internal side. The thickness of the tetrahedral

Si sheet, measured from the weighted mean oxygen positions, is 0.226 nm, and that of the octahedral Mg sheet 0.208 nm, which corresponds to a combined layer of 0.434 nm (Wicks and O'Hanly, 1988). The combined d of 0.434 nm is smaller than the layer separation distance of 0.73 nm. The length of the c-axis, 1.46 nm, measures two basal Mg-Si sheet distances of 0.73 nm. The 0.73 nm layer thickness has also been determined by electron microscopy on Ni-containing garnierite (Scholten et $al.$, 1975), which is structurally equivalent to chrysotile. The circle of connected unit cells of chrysotile in the b-direction is always an integer (n) of b_s and b_b (Eqs. 10 and 11):

$$2\pi R_i = n b_s \qquad \text{(nm)} \qquad (10)$$

$$2\pi (R_i + d) = n b_b \qquad \text{(nm)} \qquad (11)$$

where R_i is the inner radius of curvature, d the effective thickness of the Si-Mg layer of 0.434 nm, and b_s and b_b are the cell parameters of the silica and brucite sheet. Eq. 10 subtracted from Eq. 11 yields Eq. 12:

$$2\pi d = n(b_b - b_s). \qquad \text{(nm)} \qquad (12)$$

Finally, the division of Eq. 10 by Eq. 12 results in:

$$R_i = d b_s/(b_b - b_s)$$

$$= 0.43 \cdot 0.87/(0.94 - 0.87) = 5.3. \qquad \text{(nm)} \qquad (13)$$

A similar calculation can be made for a bending in the a-direction with the result, $R_i = 5.4$ nm. Calculation with bending in the a·b diagonal with length $\sqrt{(a^2 + b^2)}$ gives the result $R_i = 5.4$ nm. The inner radius is smaller than the theoretical value of 5.3–5.4 nm, since the theoretical radius is situated within the tube wall. The molar ratio Mg/Si of 3/4 in talc is half that of chrysotile. In talc, the brucite sheet is bonded to two silica sheets, and talc will form plates. Thermoporometry should detect the absence of pores of talc platelets, and the validity of the method can be checked.

In addition to checking the thermoporometric technique, additional aims of the paper are: 1) the description of the hydrothermal synthesis of the serpentine minerals with molar Mg/Si ratios of 3/1.5, 3/2 (chrysotile), 3/3.6, and 3/4 (talc), from two different silica sources, sodium silicate and fumed silica powder (Aerosil, Degussa, BRD); 2) characterization of the reaction products with X-ray diffraction (XRD); and 3) investigation of the pore structure of the dried samples with transmission electron microscopy (TEM) and nitrogen sorption. Additionally, diffuse reflectance infrared fourier transformed spectroscopy (DRIFTS) offers the possibility to monitor the curvature of the tube wall and measure the existence of adsorbed water on the clays. Adsorbed water may affect the size of the ice-crystals formed in the tubes. Finally, the measured pore radii, volumes, and surface areas obtained by thermoporometry, TEM, and N_2 sorption will be compared.
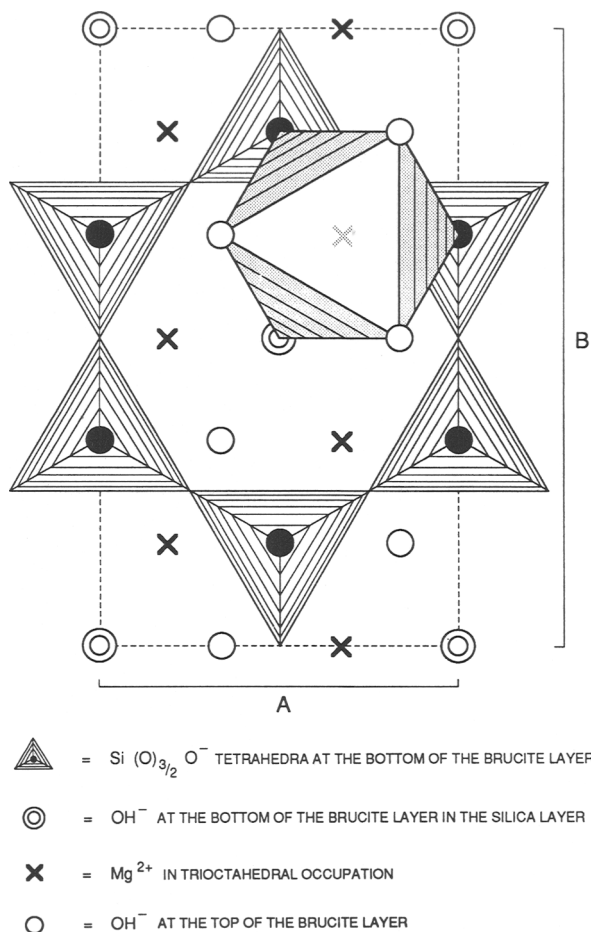

△ (Si tetrahedra)	= Si $(O)_{3/2}$ O^- TETRAHEDRA AT THE BOTTOM OF THE BRUCITE LAYER
◎	= OH^- AT THE BOTTOM OF THE BRUCITE LAYER IN THE SILICA LAYER
✕	= Mg^{2+} IN TRIOCTAHEDRAL OCCUPATION
○	= OH^- AT THE TOP OF THE BRUCITE LAYER

Figure 6.　Projection of the monocline unit cell of clinochrysotile in the a × b plane.

EXPERIMENTAL METHODS

Hydrothermal synthesis

$Sodium$ $silicate$ $(S$ $series)$. A stock 2.5 M magnesium chloride solution is prepared. A 3.5 M SiO_2, 1.5 M Na^+ Si-containing solution is obtained by diluting Merck sodium silicate solution ART 5621 with water in a 1/1 volume ratio. Amounts of 200 ml of the Mg-solution with appropriate amounts of Si-solution are mixed, yielding Mg/Si molar ratios of 3/1.5, 3/2, 3/3.6, and 3/4 (Table 1). To provide a molar ratio Na-to-Cl of 1, additional NaOH (Merck, art. 6498) is added to the suspensions S1–S4.

$Fumed$ $silica$ $(A$ $series)$. Appropriate amounts of Aerosil 380 powder (Degussa, BRD) for the above ratios are dissolved into 100 ml of a hot 2.5 M NaOH solution of 393 K. The Si-containing solutions thus prepared are cooled and added to 50 ml of the stock $MgCl_2$ solution, yielding suspensions with ratios identical to the series S (Table 1).

$Procedure$. Aliquots of 110 g of the suspensions S1–S4

Table 1. Composition of the starting Mg and Si-containing solutions, and conditions of hydrothermal treatment.

Sample	ml.A[1]	ml.B[2]	Addition of NaOH	pH	Ratio Mg/Si	T(K)	P (hPa)
Sodium silicate							
S1	200	72	328 ml 2.8 M	11.1	3/1.5	568	80
S2	200	96	304 ml 3.0 M	11.1	3/2	600	120
S3	200	174	226 ml 3.7 M	10.6	3/3.6	563	75
S4	200	192	208 ml 3.8 M	10.6	3/4	573	85
	ml.A	Silica in 2.5 M NaOH g SiO_2/100 ml		pH	Ratio Mg/Si	T(K)	P (hPa)
Fumed silica (Aerosil)							
A5	50	3.8		10.4	3/1.5	568	80
A6	50	5.0		10.4	3/2	600	120
A7	50	9.1		9.6	3/3.6	563	75
A8	50	10.0		9.6	3/4	573	85

[1] A = 510 g $MgCl_2 \cdot 6H_2O$ in 1 liter H_2O; 2.5 M Mg^{2+} and 5 M Cl^-.
[2] B = Stock sodium silicate solution; 3.5 M SiO_2 (0.21 g SiO_2/ml) and 1.5 M Na^+.

and A5–A8 are placed in 225 ml Teflon tubes of a diameter of 4 cm. The Teflon tubes are closed at both sides with Teflon plugs and outer steel clamps. Two tubes are treated simultaneously in a 2 liter stainless steel vessel. Distilled water (750 ml) is added to the bomb outside the tubes to provide an equal water vapor pressure inside and outside the tubes. The bomb is externally heated for 24 hr at temperatures ranging from 563 to 600 K, yielding hydrostatic pressures between 80 and 120 hPa. After treatment, the bomb is slowly cooled and the magnesium silicate suspensions

are centrifuged for 10 min at 5000 rpm. The residues are re-suspended in water, washed, and centrifuged for 10 min at 5000 rpm to remove excess sodium. Any possible leaching during washing with distilled water was not investigated. The last procedure is repeated twice. Finally, the synthetic clay is dried for 24 hr at 393 K and powdered.

Analytical techniques

Powder XRD reflections are recorded on a Guinier-Johansson camera ($CuK_{\alpha1}$ radiation 1.5406 Å). TEM micrographs and electron diffraction patterns are recorded with a Philips EM 420 transmission electron microscope. TEM samples are prepared by suspending the clay in ethanol with ultrasonic treatment. A droplet of the suspension is placed on a holey carbon film supported on a copper grid and air dried. The electron diffraction maxima in TEM are measured as the radial distances, l, on the film in mm from the position of the incident electron beam on the film. The lattice plane distances d in Å are inversely proportional to the radial distances, l, in mm, with a constant of $11.9 \cdot 10^{-13}$ m² being unique to the camera. A gold film is used as reference. The diffraction points are indexed using Eq. 14 of clinochrysotile with the angle β of 93° (Brown, 1961; Zussman *et al.*, 1957).

$$1/d^2 = \langle 1/d, 1/d \rangle$$
$$= h^2/a^2 \sin^2\beta + k^2/b^2 + l^2/c^2 \sin^2\beta$$
$$- 2 \, hl\cos\beta/ac\sin^2\beta \ (\text{Å}^{-2}). \quad (14)$$

The projection of the clustered hollow needles of, e.g., sample S2 in the b and c plane is reconstructed in Figure 7, showing the fiber radius, R_f, the intra radius, R_i, and the derived inter-particle radius, R_o, assuming each needle is surrounded by six others (Fripiat and della Faille, 1967). This projection of serpentine was actually photographed in work of Wicks *et al.* (1988). The derived internal and external pore volume, $V_{p,i}$
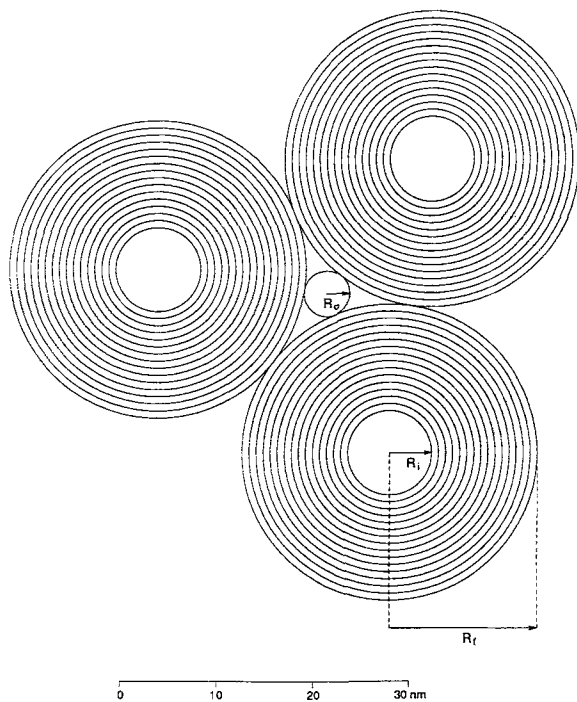

Figure 7. Projection of the hexagonal closed packing of chrysotile needles of S2 in the b × c plane. R_f is the radius of the fibres, R_i the internal radius, and R_o the external radius.

Table 2. Porous structure of chrysotile by transmission electron microscopy.

Sample	S1	S2	A5	A6
Length of the tubes (μm)	0.1–0.2	1–2	0.1–0.2	1–2
Diameter tubes $D_f (2 \cdot R_f)$ (nm)	37	31	21	36
Inner tube radius R_i (nm)	3	4.5	2.5	4
Inter tube radius R_o[1]	2.9	2.4	1.6	2.8
Thickness of the wall δ (nm)	15	11	8	14
Number of sheets in wall	21	15	11	19
Internal porosity $V_{p,i}$ (ml/g)[2]	0.01	0.04	0.02	0.02
External porosity $V_{p,o}$ (ml/g)[3]	0.04	0.04	0.04	0.04
Total porosity $V_{p,i+o}$ (ml/g)	0.05	0.08	0.06	0.06
Internal area $A_{s,i}$ (m²/g)[4]	7	16	19	10
External area $A_{s,o}$ (m²/g)[5]	43	54	78	45
Total surface area (m²/g)	50	70	97	55
Radius tube R_f (nm)	18.5	15.5	10.5	18
α, distance not available to N_2[6]	2,39	2,17	1,75	2,35
$A_{s,o}^{*}$ (m²/g), external surface area available to N_2[7]	38	47	66	39
Total surface area available to N_2	45	63	98	49

[1] $R_o = ((2/\sqrt{3}) - 1) \cdot R_f$.
[2] $V_{p,i} = R_i^2/2.58 \cdot (R_f^2 - R_i^2)$ (ml/g).
[3] $V_{p,o} = (2\sqrt{3} - \pi) \cdot R_f^2/(\pi \cdot 2.58 \cdot (R_f^2 - R_i^2))$ (ml/g).
[4] $A_{s,i} = 2 \cdot 10^3 \, V_{p,i}/R_i$ (m²/g).
[5] $A_{s,o} = A_{s,i} \cdot R_f/R_i$.
[6] $\alpha = -r_N + \sqrt{(r_N^2 + 2 \cdot r_N \cdot R_f)}$, $r_N = 0.177$ nm.
[7] $A_{s,o}^{*} = A_{s,o} \cdot (1 - (6\alpha/2\pi R_f))$.

and $V_{p,o}$, and the internal and external surface area, $A_{s,i}$ and $A_{s,o}$, are calculated with the formulae 1) $R_o = [(2/\sqrt{3}) - 1] \cdot R_f$; 2) $V_{p,i} = R_i^2/2.58 \cdot (R_f^2 - R_i^2)$ (ml/g); 3) $V_{p,o} = (2\sqrt{3 - \pi}) \cdot R_f^2/[\pi \cdot 2.58 \cdot (R_f^2 - R_i^2)]$ (ml/g); 4) $A_{s,i} = 2 \cdot 10^3 \, V_{p,i}/R_i$ (m²/g); 5) $A_{s,o} = A_{s,i} \cdot R_f/R_i$ (Table 2). Furthermore, nitrogen cannot penetrate in the regions, α, where the distance between the walls of the two adjacent chrysotile tubes is smaller than the molecular diameter of nitrogen, i.e., 0.354 nm. The region, α, is expressed in the radius of nitrogen, r_N of 0.177 nm, by $\alpha = -r_N + \sqrt{(r_N^2 + 2 \cdot r_N \cdot R_f)}$. Each tube is surrounded by six others and has $6 \cdot 2 = 12 \, \alpha$ areas. Each area is counted double by two tubes, which delivers 6 α areas. The external surface area available to N_2, $A_{s,o}^{*}$, is $A_{s,o} \cdot [1 - (6\alpha/2\pi R_f)]$, and the total surface area available to N_2 is $A_{s,i} + A_{s,o}^{*}$ (Tables 2 and 3). With calculation of the pore characteristics from TEM images, a grain density of 2.58 g/ml of the chrysotile wall is used. The density is calculated with Eq. 15:

$$D = 4 \times Mw \; Mg_3(Si_2O_5)(OH)_4/N_{av} \cdot a \cdot b \cdot c \cdot \sin \beta$$

$$= 2.58 \; (g/ml) \tag{15}$$

where Mw $Mg_3(Si_2O_5)(OH)_4$, the molar weight of chrysotile, is 277.1 g/mole, N_{av}, the Avogadro number ($6.02 \cdot 10^{23}$ mole^{-1}), and $\langle[axc],b\rangle = a \cdot b \cdot c \cdot \sin \beta$, the volume of the unit cell, which is $7.13 \cdot 10^{-24}$ ml.

Thermoporometry

A suspension of about 100 mg clay in 0.2 ml H_2O (in an aluminum cup) is cooled in a Setaram 111 differential scanning calorimeter (DSC) from 293 to 220 K at a cooling rate of 0.5 K/min. The heat-flux during the solidification of water is recorded as a function of the temperature. Due to supercooling of bulk water present outside the pores of the solid, the heat of solidification is measured at about 264 K, as recorded in the thermogram (Charoenrein and Reid, 1989). In order to avoid the supercooling of bulk water, the sample is subsequently heated at a rate of 0.5 K/min from 220 to 265 K, just below the melting point of bulk water at 273 K. The heat-flux during melting of the ice in the pores is recorded. Finally, the sample is cooled a second time from 265 to 220 K, and the heat involved with solidification of water within the pores is exclusively measured.

N_2 adsorption and desorption and DRIFTS

The samples S1, S2, A5, and A6 are evacuated for 6 hr at 473 K under vacuum before N_2 is adsorbed employing a Carlo Erba Omnisorp (TM) 100. The BET surface areas and pore volumes are calculated from the N_2 adsorbed isotherm, using a surface area of 16.2 Å²

Table 3. The total surface area available to N_2 determined by TEM compared with the BET surface area obtained by nitrogen sorption.

Sample	Total surface area available to N_2 by TEM	BET surface area by nitrogen sorption
S1	45	46
S2	63	54
A5	98	87
A6	49	63

for a physically adsorbed N_2 molecule. The pore size distribution is calculated from the desorption isotherm according to the formula of Lowell and Shields (1984). The infrared absorption spectra in the range 4000–450 cm^{-1} of the finely powdered clays S1–S4, A5–A8 (25 wt. % in KBr) are measured on a Perkin Elmer FT-1720 in combination with a spectra-tech diffuse reflectance accessory collector. DRIFTS shows two types of vibrations, in the range of 4000 to 2000 cm^{-1} OH-stretching vibrations and in the range of 1225 to 450 cm^{-1} lattice vibrations.

RESULTS

XRD and TEM

The reaction products S1, S2, A5, and A6 are identified by XRD as a mixture of chrysotile and brucite. A7 and A8 are identified as talc, and S3 and S4 as amorphous product (Table 4). Brucite in the samples S1, S2, A5, and A6 is measured by XRD, which may introduce additional macropores in the system. TEM micrographs and an electron diffraction pattern of S1 in Figure 8 clearly demonstrate the fibrous morphology of chrysotile. The electron diffraction pattern of S1 displays h00, 0k0, 00l, hk0, h0l reflections, but no hkl and 0kl reflections. The 0k0 and 00l reflections are located on a line, which illustrates the bending of the layers. No traces of brucite are seen, but brucite may be present as a few large crystals, probably with pores >5 nm. Drying brings about a parallel orientation of the needles. Though the inner diameter is likely to have a Gaussian frequency distribution curve (Fripiat and della Faille, 1967) the inner diameter is averaged from several needles on different TEM micrographs and taken as the most probable internal diameter. The internal diameter D_i is 6 nm and the external diameter D_f is 37 nm for S1. The textural parameters obtained by TEM of S1, S2, A5, and A6 are given in Table 2. The needles of S1 have a length of 0.1–0.2 μm (Figure 8), which is about ten times shorter than the 1–2 μm observed for S2 (Figure 9). Low Mg/Si molar ratios of 3/1.5 yield short chrysotile with a length of 0.1–0.2 μm, while the 3/2 ratio corresponding to chrysotile yields long tubes of 1–2 μm. Amorphous sol particles, probably silica, incorporated in the hollow tubes of S1, might occur because the silica sheet is at the inner side of the chrysotile tubes. The sol particles seem to bear a surface charge and are usually separated by a distance of about 22 nm.

In the TEM micrographs and the electron diffraction pattern of S2 (Figure 9), with the Mg/Si molar ratio corresponding to chrysotile, parallel oriented needles are again seen. The irregular spiral shape of some particles of S2 and of A6 (Figure 11) indicates a rotation axis in the direction of the fiber axis a-direction. This implies that the curvature model with bending only in the b-direction is oversimplified.

In Figure 10, the TEM micrographs of A5 with molar Mg/Si ratio identical to S1 illustrate that the length of the needles is also comparable to S1 (Table 2). Fortunately, one of the needles is oriented perpendicular on the copper grid, which causes the tubular shape to be clearly visible at the arrow. Small talc crystals of A7 display no tubular morphology (Figure 10). The talc crystals of A7 remain small due to the absence of bending to relieve stress. A Mg/Si ratio of 3/3.6 and 3/4 leads to platy talc crystals. Sample A6 with the same molar Mg/Si ratio as S2 contains chrysotile needles of 1–2 μm length (Figure 11).

Thermoporometry

The amount of water present within the pores can be deduced from the thermograms of pure chrysotile, e.g., S2 and A5 in Figure 12 (the position of the curves does not represent an absolute value of the heat-flux due to vertical displacement of the curves). In the first cooling step, S2 exhibits a large exothermic solidification peak at 265 K of supercooled bulk water (1), and a much smaller exothermic solidification peak at 255 K of pore water (2, Figure 12A). The freezing point depression, dT_s, is 18.3 K. The melting peak of the ice present within the tubes is registered during the heating step at 256.6 K (3). The 'fusion point' depression, dT_f, of the melting of ice within the tubes is 16.6 K. The shape factor, F, is therefore $18.3/16.6 = 1.1$, which is assumed to be characteristic for a spherical pore shape. During the second cooling cycle, a solidification peak of pore water is observed at 255 K (4). The ice-crystal radius R_n of S2 corresponding to the maximum of heat-flux is 3.3 nm (Eq. (2)).

The thermogram of chrysotile A5 in Figure 12B displays the solidification peak of pore water at 251.8 K (2) with $dT_s = 21.5$ K; and during the heating step, an endothermic fusion peak at 257.9 K (3) with $dT_f = 15.4$ K. The shape factor F of A5, which is $21.5/15.4 = 1.4$, is large compared with the value of 1.1 for S2, which may imply that the ice-crystals grow more cylindrically.

Macropores appear as shoulders on the bulk peak at 273 K during the final heating step. Due to the overlap with the peak of bulk water at 273 K, no V_n for these peaks can be determined. The shoulder and bulk peak are not displayed in Figure 12, due to the dominant heat-flux involved with fusion of the bulk water. The peak due to the macropores for A5 has its maximum at 268 K, with a dT_f of -5.2 K, corresponding to a value for R_n of 6.1 nm.

The thermoporometric pore radii of the samples S1, S2, A5, and A6 range from 2.8 to 3.3 nm, and the pore volumes, V_n, from 0.016 to 0.02 ml/g (Table 5). Figure 13 displays the pore size distribution curves of S2 and A5, which are derived from the thermograms in Figure 12. The pore size distribution curve is a Gaussian distribution curve as earlier observed by Fripiat and della
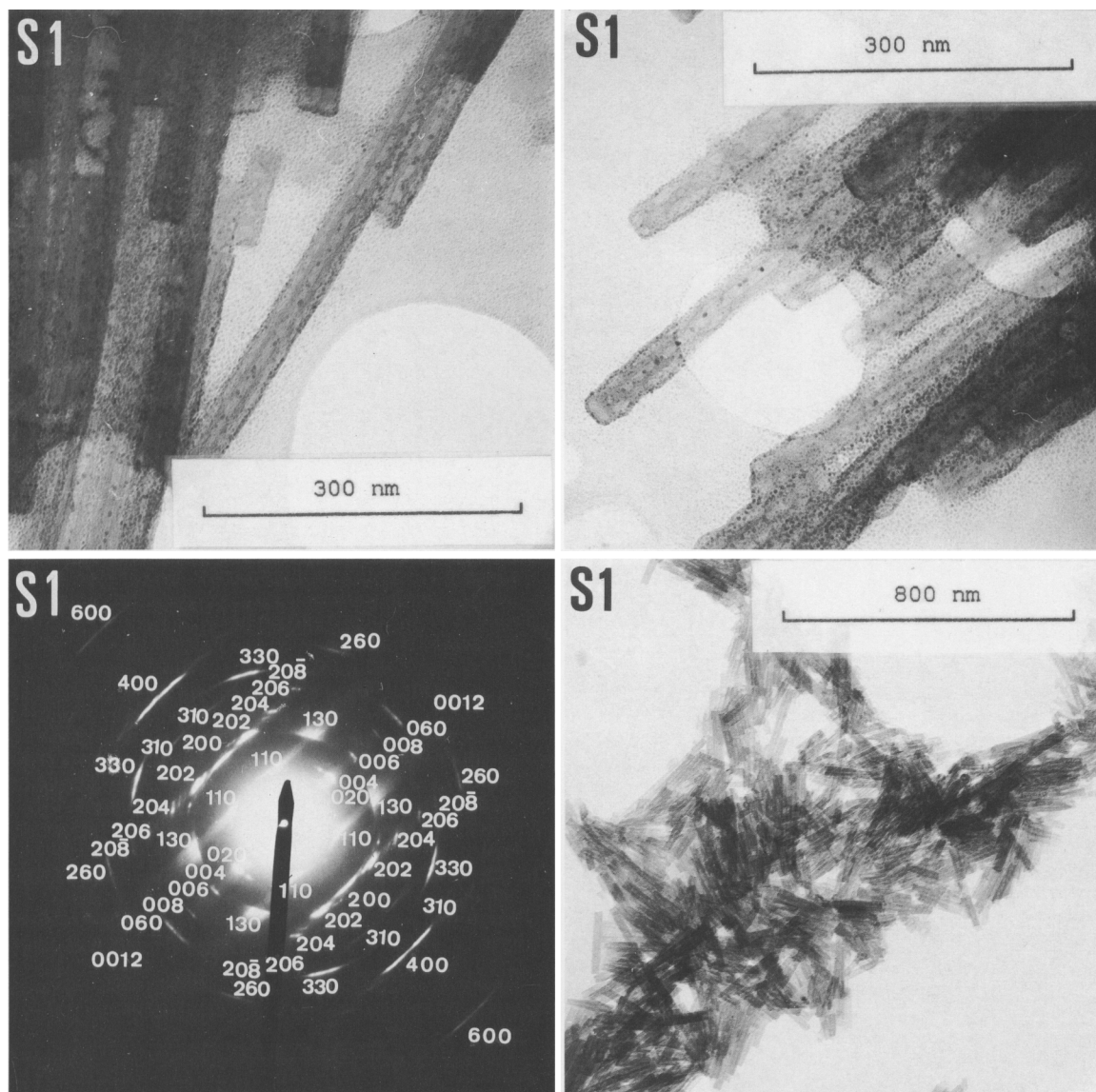
Figure 8.   TEM micrographs and an electron diffraction pattern of S1 (chrysotile).

Faille (1967) for the outside diameter of the tubes. The pore volume presented by the surface area under the curves is normalized on 1. Sample S2 displays a broad pore size distribution with a maximum at 3.3 nm. A small shoulder is observed at 2.8 nm. The curve of the sample A5 shows a sharp peak with a maximum at 2.8 nm.

Water present within pores is not detected with the talc samples S3, S4, A7, and A8. The thermograms are, therefore, not displayed in this paper.

N_2 adsorption and desorption

The pore characteristics of S1, S2, A5, and A6 are summarized in Table 6. The pore size distribution of S2 in Figure 14A exhibits three main peaks; a large peak at 3.2 nm (1), an additional peak at 2.3 nm (2), and a broad peak at 16 nm (3). The same type of pore size distribution exists in A5 (Figure 14B), but the peaks are shifted towards smaller dimensions, i.e., 2.8 (1), 1.8 (2), and 5 nm (3). Due to the more compact character of the needle aggregates, the pore size distribution of the macropores at 5 nm (3, Figure 14B) is smaller than that of S2 (Figure 14A).

DRIFTS

The DRIFT spectra of the samples S1–S4 and A5–A8 are represented in Figures 15A and 15B, respectively. Samples S1, S2, A5, and A6 are identified as chrysotile, A7 and A8 as talc, and S3 and S4 as amorphous silica. Broad absorption bands of adsorbed water
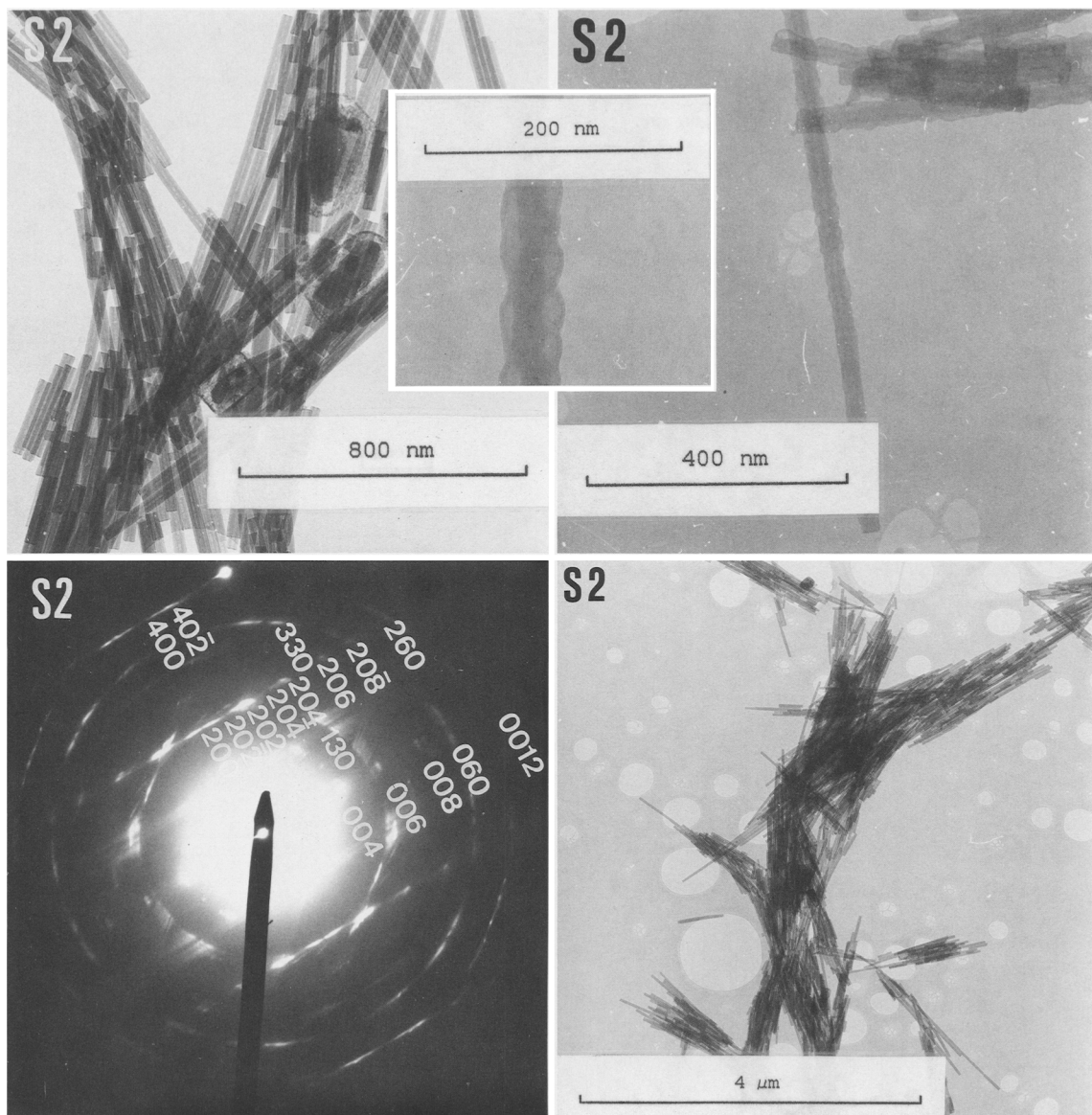
Figure 9.   TEM micrographs and an electron diffraction pattern of S2 (chrysotile).

are observed between 3000 and 3500 cm^{-1} and at 1635 cm^{-1} in all spectra.

The chrysotile samples S1, S2, A5, and A6 have two characteristic MgOH stretching vibrations at 3688 cm^{-1} and 3638 cm^{-1} (Figure 15A) attributed to the three external OH at the top of the brucite sheet, and one internal OH at the bottom of the brucite sheet (Jolicoeur and Duchesne, 1981). The intensity ratio of the peaks is predicted to be 3/1. The single, sharp peak at 3695 cm^{-1} of talc A7 and A8 in Figure 15B is due to the single internal MgOH-stretching vibration. In talc, all hydroxyls are equivalent. The internal OH-stretching vibration at 3695 cm^{-1} is located at about the same wavenumber as the external OH-stretching vibration of chrysotile.

The absorption bands at about 1081 cm^{-1}, 1010 cm^{-1}, and 947 cm^{-1} (Figure 15A) are typical for the Si-O-Si stretching vibrations of the silica network (Yariv and Heller-Kallai, 1975; Luys *et al.,* 1982). The 1081 cm^{-1} band is attributed to the out-of-plane symmetric stretching vibration of the silica sheet. The degeneracy of the single band at 1010 cm^{-1} in talc to two bands at 1010 cm^{-1} and 947 cm^{-1} in chrysotile is explained by the bending of the silica sheet. The 1010 cm^{-1} band is attributed to Si-O-Si stretching vibrations, mainly parallel to the b-axis in the direction of the curvature, while the 947 cm^{-1} is due to Si-O-Si stretching vibrations parallel to the a-axis. The relative intensity of both bands is affected by ultrasonic treatment of chrysotile (Yariv and Heller-Kallai, 1975).

Table 4.　X-ray powder diffraction data of hydrothermally prepared samples.

Chrysotile, monoclinic a = 5.32 Å, b = 9.17 Å, c = 14.64 Å, β = 93° (JCPDS file No. 25-645)

Sample	S1	I/I₁	S2	I/I₁	A5	I/I₁	A6	I/I₁	ref[1]	I/I₁	hkl
d(Å)	7.39	100	7.39	100	7.52	100	7.41	100	7.36	100	002
	4.56	55	4.56	50	4.48	35	4.56	30	4.56	50	020
	3.68	75	3.68	60	3.68	50	3.68	60	3.66	80	004
	2.66	25	2.66	10	—	—	2.66	20	2.66	30	200
	—	—	—	—	—	—	2.60	15	2.60	40	201
	—	—	2.54	20	2.57	—	—	—	2.53	—	20–2
	2.46	>I₁	2.49	>I₁	2.46	—	2.46	>I₁	2.50	50	202
	2.28	50	—	—	—	—	2.22	30	2.29	20	040
	2.07	40	2.10	20	2.03	—	2.10	20	1.97	20	205
	—	—	1.75	25	—	—	1.80	15	1.83	30	008
	1.54	95	1.54	80	1.53	65	1.54	70	1.53	65	060
	1.31	60	1.32	30	1.31	30	1.32	40	1.31	40	402

Talc, monoclinic a = 5.29 Å, b = 9.17 Å, c = 18.96 Å, β = 99°61′ (JCPDS file No. 19-770)

Sample	S3	I/I₁	S4	I/I₁	A7	I/I₁	A8	I/I₁	ref[1]	I/I₁	hkl
d(Å)	—	—	—	—	9.54	100	9.65	100	9.35	100	002
	—	—	—	—	4.58	>I₁	4.56	60	4.59	45	020
	—	—	—	—	2.60	<I₁	2.60	30	2.60	20	13–2
	—	—	—	—	2.49	<I₁	2.51	50	2.50	20	13–3
	—	—	—	—	1.53	>I₁	1.53	65	1.53	55	060

Brucite, hexagonal a = 3.147 Å, c = 4.769 Å (JCPDS file No. 7-239)

Sample	S1	I/I₁	S2	I/I₁	A5	I/I₁	A6	I/I₁	ref[1]	I/I₁	hkl
d(Å)	4.76	50	4.77	35	4.77	40	4.79	30	4.77	90	001
	—	—	—	—	—	—	—	—	2.73	6	100
	2.37	100	2.37	100	2.37	100	2.37	100	2.37	100	101
	1.80	35	1.80	45	1.79	45	1.80	40	1.79	55	102
	1.58	30	1.58	30	1.57	30	1.58	30	1.57	35	110
	1.50	20	—	—	1.50	15	—	—	1.49	18	111
	1.38	10	—	—	—	—	—	—	1.37	16	103
	—	—	—	—	—	—	—	—	1.36	2	200
	1.31	15	—	—	—	—	—	—	1.31	12	201

[1] JCPDS.

The small peak at 1202 cm⁻¹ for S1, S2, A5, and A6 represents small traces of amorphous silica. The absorption band of the Mg-O stretching vibration at 670 cm⁻¹ of octahedrally coordinated Mg (A7 and A8) is shifted to a lower wavenumber of 655 cm⁻¹ (A5 and A6). The Mg-O stretching vibration band at 660 cm⁻¹ is the same for the talc samples, S3 and S4, and the chrysotile samples, S1 and S2.

DISCUSSION

General

The heat-flux measured by thermoporometry originates from water present within the hollow chrysotile tubes, which is supported by the absence of an analogous heat-flux in talc. A shape factor, F, of 2 in thermoporometric characterization of a cylindrical pore shape should be expected for the chrysotile samples. However, lower shape factors between 1.1 and 1.4 are experimentally measured (Table 5). The shape factors are even smaller than the minimum value of 1.4 that Jallut et al. (1992) reported for a matrix of compacted alumina grains approximating spherical pores. The ice

crystals remain spherical after solidification. Cylindrical shapes may be obstructed by the presence of amorphous sol particles in the tubes (Figure 8). There may be no continuity of frozen water within the pores because of amorphous material within the tubes (Fripiat and della Faille, 1967), and the ice-crystals grow spherical to form a chain of crystals. The amorphous material has probably the same composition as bulk chrysotile. A second possibility is that only penetration of the ice-meniscus proceeds according to the model of Enüstün et al. (1990). The retreat of the ice-meniscus in the uniform pore with thawing occurs at the same temperature, resulting in a shape factor of nearly 1.

The DRIFTS absorption bands at 3000–3500 cm⁻¹ and at 1635 cm⁻¹ are attributed to the stretching and bending vibration of water and are especially strong for S3 and S4, which implies that water is bound to silica in the chrysotile structure (Suquet, 1989). The absorption bands are especially strong in 100% leached samples and assigned to water adsorbed on Si-OH groups. Water adsorbed on silica may form a nonfreezing layer with a thickness of 0.9 nm. The ice-crystal radius R_n is expected to be 0.9 nm smaller than
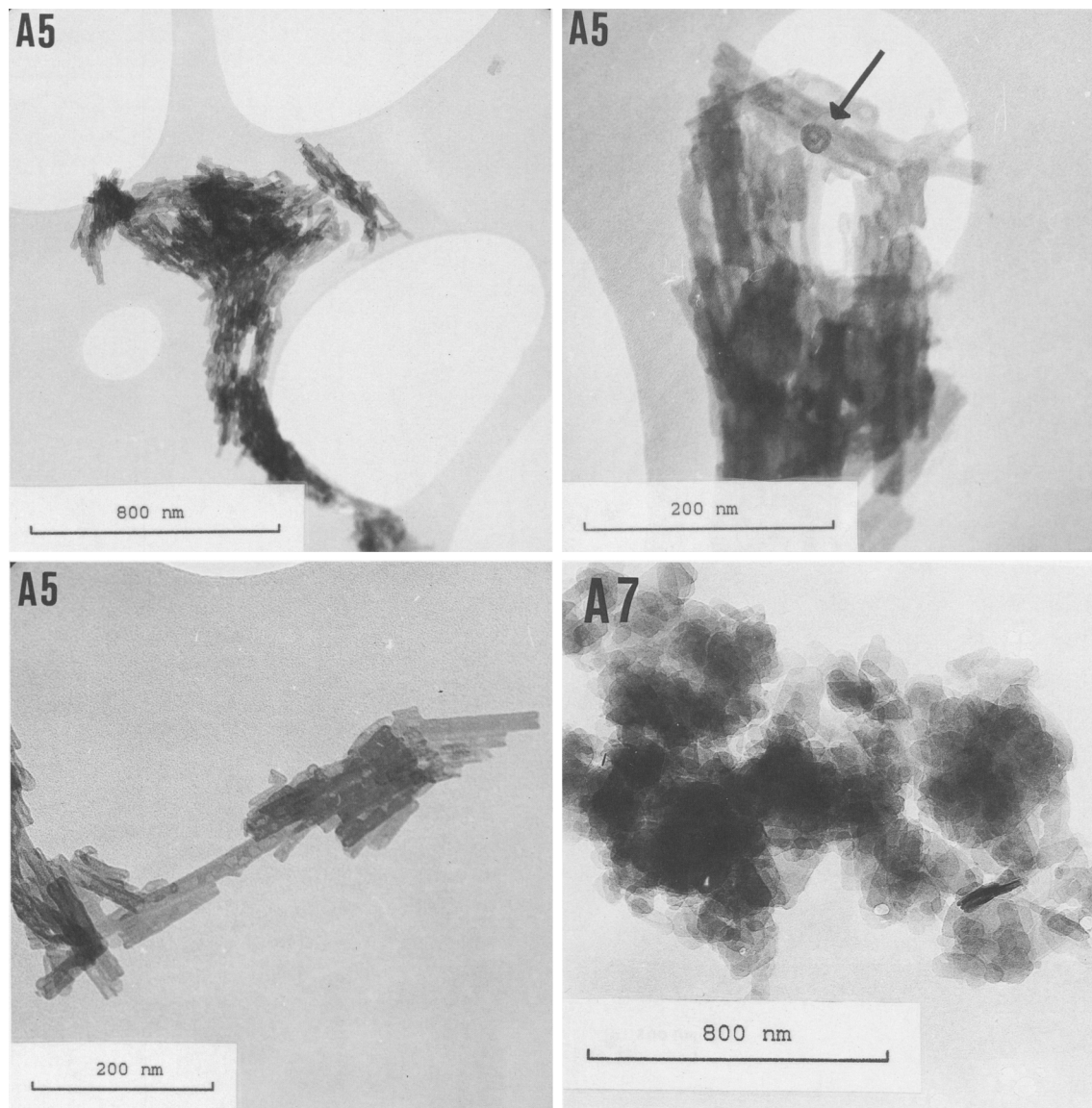
Figure 10.   TEM micrographs of the A5 (chrysotile) and A7 (talc).

the pore radius R_p. The existence of such a layer in chrysotile can be verified by comparison of the thermoporometric results to the N_2 adsorption and desorption results.

The N_2 pore radius distribution curves of two chrysotile samples, S2 and A5, (Figure 14) can be explained using Figure 7. The peak (1) at about 3 nm is ascribed to the internal radius R_i of the tubes; the peak (2) at about 2 nm to the inter-particle radius R_o between the tubes (the size of R_i is larger than R_o); and the peak (3) between 4 and 100 nm to macropores between the chrysotile clusters or to pores in amorphous silica or brucite. The comparison of the pore characteristics of the chrysotile tubes obtained by the three methods

TEM, H_2O (thermoporometry), and N_2 can be split into three areas: 1) the pore size distribution, 2) the pore volume, and 3) the (internal) surface area.

Pore size distributions

The pore size distribution curves of S2 and A5 obtained by thermoporometry (Figure 13) can be compared directly to the N_2 adsorption and desorption curves (Figure 14). The maxima of the broad peak of S2 and the sharp peak of A5 at 3.3 and 2.8 nm, respectively, correspond to the main peak (1) of N_2 adsorption and desorption. A very good agreement exists between the main peak radius, R_p (1), as calculated from N_2 adsorption and desorption, and the thermo-
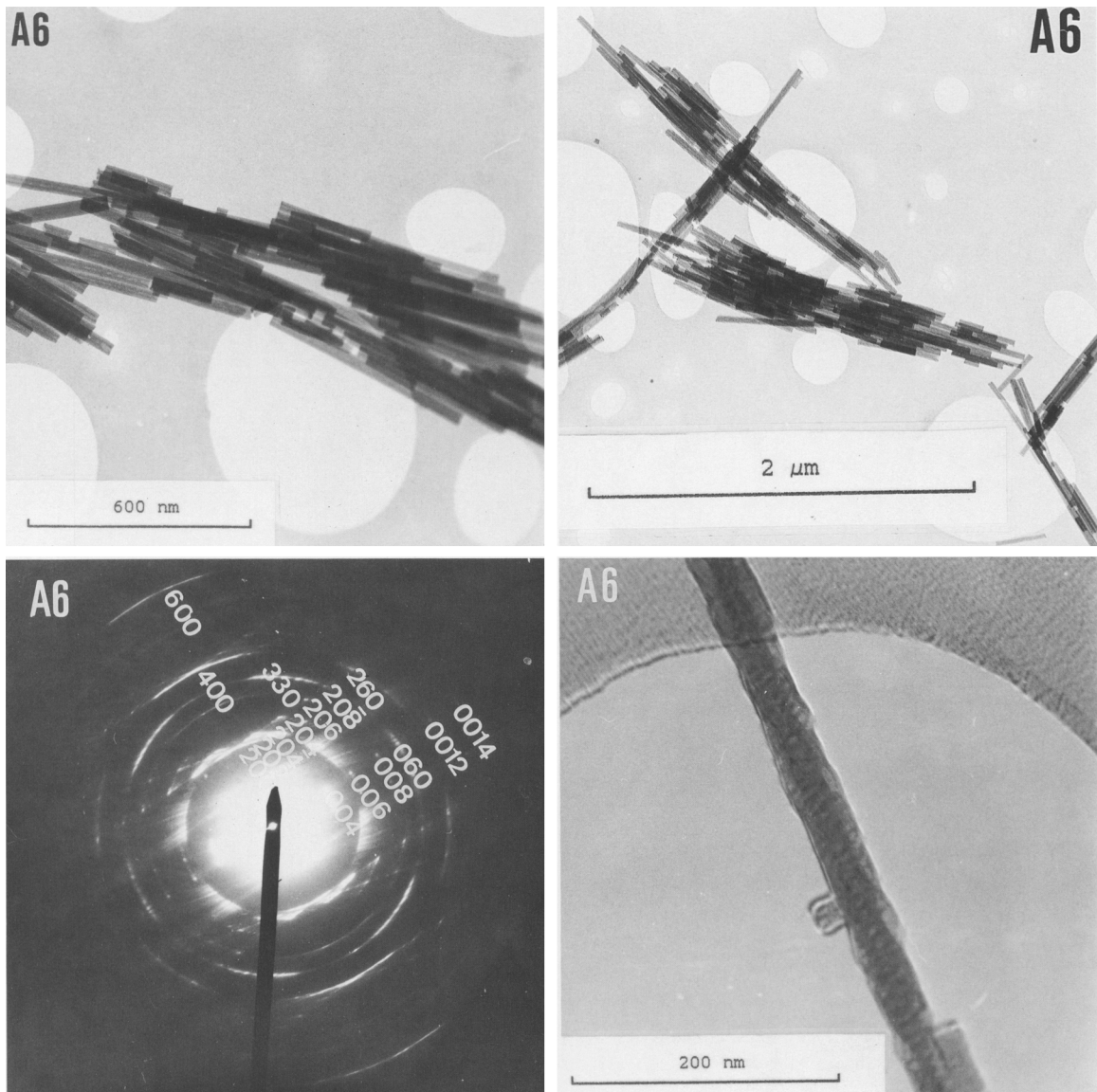
Figure 11.   TEM micrographs and an electron diffraction pattern of A6 (chrysotile). The photograph, which is rather astigmatic, shows the spiral shape of the chrysotile tubes.

porometric radius R_n (Table 7). The agreement indicates that the main peak in the desorption isotherm corresponds to the ice-crystal radius R_n. Surprisingly, the pore radius R_p is not 0.9 nm larger than the ice-crystal radius R_n, which is usually observed with amorphous silica (Jallut *et al.*, 1992). Probably all the silanol groups of the silica tetrahedra point to the brucite sheet and leave no hydrogen bonds to anchor the non-freezing layer. Due to the hydrophobic character of the inner chrysotile tubes the adsorbed water measured by DRIFTS is situated elsewhere. Young and Healy (1954) suggested that the entrance to the chrysotile tubes was blocked by water plugs that could be removed by ac-

tivation at a temperature no less than 425°C. These water plugs do not fill the entire length of the capillaries. A second observation is the internal surface area exerts a lower potential field to a nonpolar molecule than the external surface area of the chrysotile tube, which may be attributed to a more hydrophobic inner surface area and a more hydrophilic external surface area of the tubes. It is interesting that Plooster and Gitlin (1971) measured a decreasing bound water layer with decreasing hydrophilous character of the surface area. Therefore, the non-freezing layer may be entirely absent at the hydrophobous inner tube surface area. The water may also be bound to the amorphous material incor-
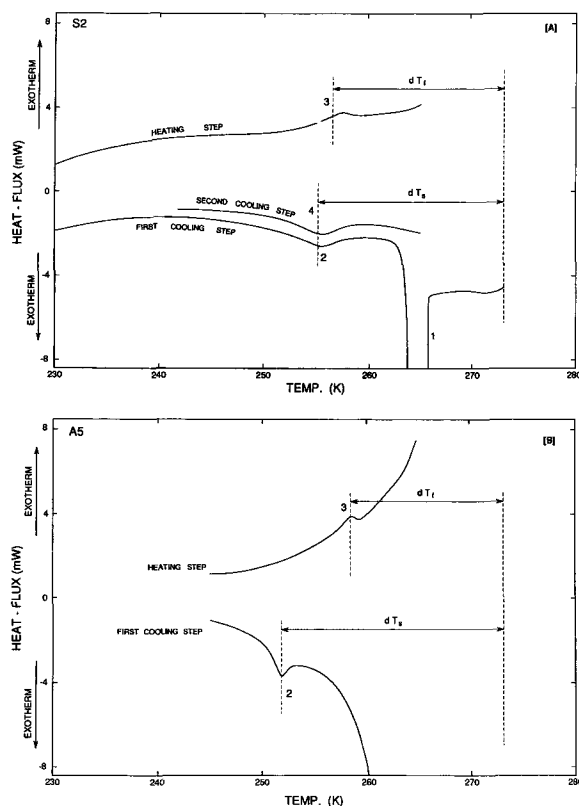
Figure 12. A) Thermograms of S2, with 9 mg solid and 273 mg H_2O, illustrating the exothermic peak of supercooled bulk water at 265 K (1), the exothermic peak of pore water at 255 K (2), the melting peak of the pore ice at 256.6 K (3), and finally, the solidification peak of pore water at 255 K the second time (4). B) A5, with 142 mg solid and 161 mg H_2O, the solidification peak of pore water at 251.8 K (2), and the endothermic fusion peak at 257.9 K (3) of pore water.
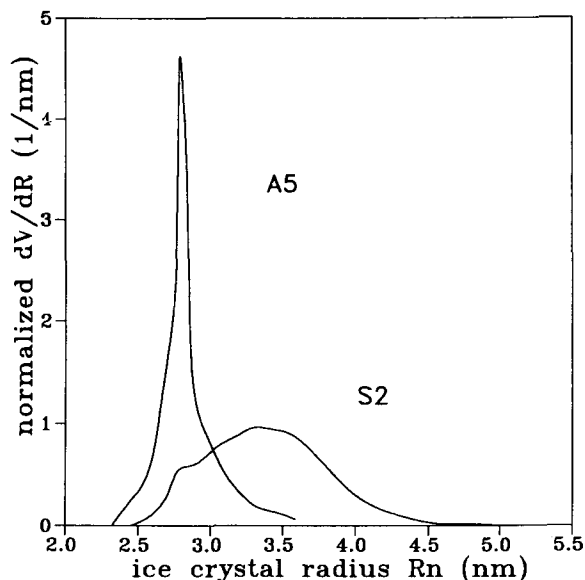

Figure 13. The heat-flux curves of S2 and A5 transformed into non-unimodal pore size distribution curves. The rather asymmetric distribution of the heat-flux curves, tailing to low temperatures, has disappeared by the reciprocal dependency of the radius, R_n, on the temperature, T_s by $R_n = -64.67/(T_s - 273.15) - 0.23$.

porated with the chrysotile tubes (Fripiat and della Faille, 1967), bound to the external surface area of the chrysotile tubes, or present as water plugs.

The secondary peak (2) of N_2 adsorption and desorption, R_o, with a smaller radius than the main peak R_i (Table 6) is not measured by thermoporometry. Perhaps, the clustering of tubes disappears when resuspended in water, and the external radius R_o between the tubes becomes too large and the signal intensity too low to be measured with thermoporometry. The shoulder on the pore size distribution curve of S2 at 2.8 nm (Figure 13) may point to the existence of some clustering in water. The third N_2 peak (3) of A5 at 5 nm (Figure 14) is attributed to macropores corresponding to the large pore size R_n of 6.1 nm determined by thermoporometry, probably of ice formed between the chrysotile clusters.

The crystal radii, R_n, obtained from thermoporometry agree well with the inner particle radii, R_i, determined from TEM micrographs (Table 7). Mostly the radii determined from TEM micrographs are slightly

larger than those obtained by thermoporometry. The radii R_n (H_2O) and R_i (TEM) exhibit an identical trend with A5 < S1 < A6 < S2.

Pore volume measurements

The thermoporometric pore volumes, V_n, of S1 and A6 are smaller than the N_2 pore volumes, $V_p(N_2)$, (1 nm < R_p < 5 nm) (Table 7), because thermoporometry determines the pore volume within the tubes, $V_{p,i}$, and not in between the tubes, whereas N_2 adsorption and desorption measures both, $V_{p,i+o}$. The thermoporometric pore volumes, V_n, of the tubes agree well with the internal pore volumes, $V_{p,i}$, calculated from TEM data (Table 7). No problems are seen with the nucleation of ice by the fairly hydrophobic inner chrysotile walls, as expected from the results of Cuperus *et al.*

Table 5. Thermoporometry applied on wet chrysotile tubes.

Sample	Cooling rate (K/h)	R_n (nm)	V_n (ml/g)	F
S1	30	3.1	0.016[1] 0.008[2]	1.1
S2	30	3.3	—	1.1
A5	30	2.8	—	1.4
A6	30	3.3	0.02[1]	1.1

[1] Cooling step.
[2] Heating step.
The amounts of solid and water are: 125 mg S1 + 190 mg H_2O, 9 mg S2 and 273 mg H_2O, 142 mg A5 and 161 mg H_2O, and 113 mg A6 and 196 mg H_2O.
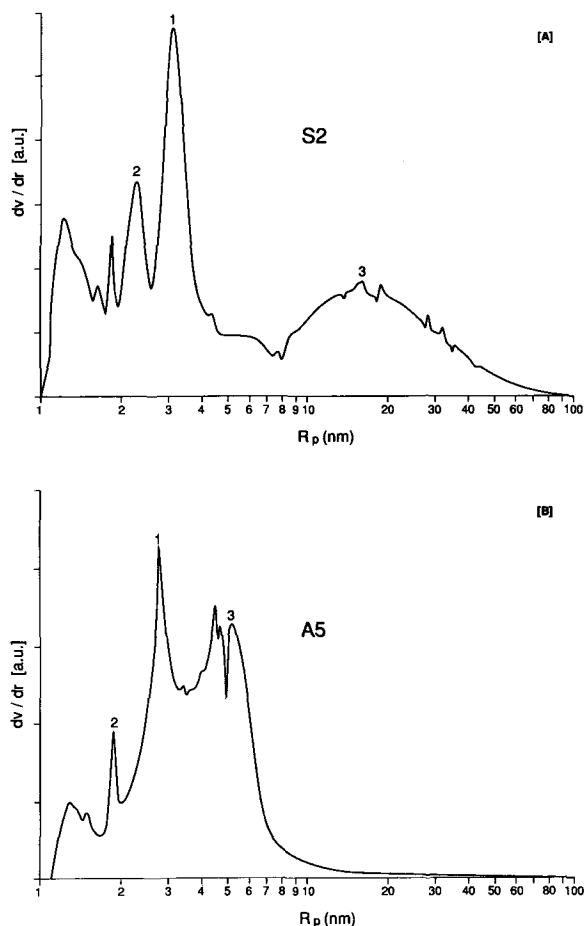
Figure 14. Pore size distribution of A) S2 (chrysotile), with a main peak at 3.2 nm (1), a secondary peak at 2.3 nm (2), and a broad peak with a maximum at about 16 nm (3); B) A5 (chrysotile), but the three peaks are shifted towards low radii, such that 2.8 (1), 1.8 (2), and 5 nm (3).

Figure 15. DRIFT spectra of A) sodium silicate samples S1–S4 and B) fumed silica (Aerosil) samples A5–A8.

(1992), resulting in very low pore volumes V_n. The pore volume, $V_{p,i+o}(N_2)$, (1 nm < R_p < 5 nm) is slightly smaller than the TEM pore volume, $V_{p,i+o}$, except with A5 (Table 7). The opposite is observed for $V_p(N_2)$ (R_p > 1 nm) (Table 6), being larger than the total TEM pore volume ($V_{p,i+o}$) (Table 7). The high N_2 pore volume is probably due to the macropore volume, which is present in pores larger than 5 nm between chrysotile clusters or in amorphous silica or brucite.

Surface area measurements

The agreement of the BET surface areas by N_2 adsorption with the surface areas calculated from the TEM images is remarkably good (Table 3). For example, the BET surface area of S1 is 46 m²/g, and the TEM surface area is 45 m²/g. The BET surface areas exhibit a similar trend as the TEM data, which is S1 < (S2, A6) < A5 (Table 3). The surface areas calculated from the N_2 desorption isotherms based on the equation $\Sigma_k 2V_{p,k}/R_{p,k}$ are about 15 m²/g larger than the BET surface areas (Table 6). The difference between the BET and N_2 desorption surface area cannot readily be explained.

Table 6. N_2 adsorption and desorption on chrysotile after evacuation for a period of 6 hr at 473 K.

Sample	R_p (nm)	V_p (ml/g)		Surface area (m²/g)	
		>1 nm	1 nm < R_p < 5 nm	BET	Desorption isotherm[3]
S1	3.2[1] 2.2[2]	0.35	0.04	46	52
S2	3.2[1] 2.3[2]	0.39	0.06	54	70
A5	2.8[1] 1.8[2]	0.25	0.13	87	115
A6	2.9[1]	0.54	0.05	63	74

[1] Main peak.
[2] Secondary peak.
[3] $A_s = \Sigma_k 2V_{p,k}/R_{p,k}$ with $R_{p,k}$ between 1 and 30 nm.

CONCLUSIONS

1) The internal pore radius, $R_{p,i}$, and pore volume, $V_{p,i}$, of chrysotile tubes can be established by ther-

Table 7. Comparison between the values obtained for $R_{p,i}$, $V_{p,i}$, and $V_{p,i+o}$, given for the different sample compositions by TEM, thermoporometry (H_2O), and N_2 adsorption and desorption.

		$R_{p,i}$			$\delta\%$	$V_{p,i}$		$V_{p,i+o}$ (1 nm < R < 5 nm)	
	Mg/Si	(TEM)	(H_2O)	(N_2)	max	(TEM)	(H_2O)	(TEM)	(N_2)
S1	3/1.5	3.0	3.1	3.2	6	0.01	0.016	0.05	0.04
S2	3/2	4.5	3.3	3.2	41	0.04	—	0.08	0.06
A5	3/1.5	2.5	2.8	2.8	11	0.02	—	0.06	0.13
A6	3/2	4.0	3.3	2.9	38	0.02	0.02	0.06	0.05

The value $\delta\%$ represents the maximal fault (in %) in the determination of R_i by the three techniques.

moporometry. The pore radii agree well with those of TEM and N_2 adsorption and desorption.

2) Water attached to silica in chrysotile and talc as established by DRIFTS does not form a layer of strongly bound water in the pores. It is likely to be present 1) as water plugs at the pore mouths, 2) as adsorbed water to the amorphous material incorporated in the hollow tubes, or 3) as water bound to the external surface of the chrysotile tubes. The water within the pores as determined with thermoporometry completely participates in the water-ice phase transformation because the internal pore radii obtained by thermoporometry and N_2 adsorption and desorption are identical.

3) The thermoporometric shape factor F of about 1 is smaller than the expected theoretical value of 2. The amorphous material incorporated in the hollow tubes may prevent the formation of one single ice cylinder, and the ice-crystals in the tubes develop as a chain of spheres. There is no continuity within the frozen water in the tubes.

4) The N_2 adsorption and desorption measurements point to a parallel orientation of clustered tubes. The value of the internal radius, R_i, and external radius, R_o, calculated from N_2 adsorption and desorption are equal to those from TEM micrographs. Furthermore, the N_2 pore volume V_p between a R_p of 1 and 5 nm is equal to that determined from TEM micrographs. The BET surface area obtained by N_2 adsorption is comparable to that obtained from TEM available to N_2.

5) Addition of water to the dried and clustered tubes probably results in the disappearance of the clustering. Thermoporometry only measures the internal radius R_i and pore volume, $V_{p,i}$, within the tubes, while TEM and N_2 adsorption and desorption provide the radii and the pore volume within and between the tubes, $R_{p,i+o}$ and $V_{p,i+o}$, respectively.

6) Comparison of radii measured by thermoporometry and either TEM or nitrogen adsorption can indicate the hydrophobicity of the surface of the porous solid, and the existence of the non-freezing layer of water.

REFERENCES

Ahlrich, J. L. and White, J. L. (1962) Freezing and lyophilizing alters the structure of bentonite gels: *Science* **136**, 1116–1118.

Anderson, D. M. and Hoekstra, P. (1965) Migration of interlamellar water during freezing and thawing of Wyoming bentonite: *Soil Sci. Soc. Amer. Proc.* **29**, 498–504.

Banin, A. and Anderson, D. M. (1971) A similar law may govern water freezing in minerals and living organisms: *Nature* **255**, 261–262.

Brown, G. (1961) *The X-ray Identification and Crystal Structures of Clay Minerals:* Mineralogical Society, Jarrold and Sons, London.

Brun, M., Lallemand, A., Quinson, J. F., and Eyraud, C. (1978) A new method for the simultaneous determination of the size and the shape of the pores: *Thermochim. Act.* **21**, 59–88.

Charoenrein, S. and Reid, D. S. (1989) The use of DSC to study the kinetics of heterogeneous and homogeneous nucleation of ice in aqueous systems: *Thermochim. Act.* **156**, 373–381.

Cuperus, F. P., Bargeman, D., and Smolders, C. A. (1992) Critical points in the analysis of membrane pore structures by thermoporometry: *J. Membr. Sci.* **66**, 45–53.

Dedyulya, I. V. and Churaev, N. V. (1988) Viscosity of nonfreezing interlayers of aqueous electrolyte solutions between ice and silicate surface: *Coll. J. USSR* **50(2)**, 232–236.

Deer, W. A., Howie, R. A., and Zussman, J. (1962) *Rock Forming Minerals, Vol. 3² Sheet Silicates:* Longmans, London, 170–190.

Ehrburger, F., Querin, V., and Lahaye, J. (1985) DTA studies of sol and gel structures in aqueous dispersions of pyrogenic silicas: *Colloids and Surfaces* **14**, 31–45.

Enüstün, B. V., Gunnink, B. W., and Demirel, T. (1990) Phase transition porosimetry and surface area determination: *J. Coll. Interf. Sci.* **134**, 264–274.

Everett, D. H. (1961) The thermodynamics of frost damage to porous solids: *Transactions of the Faraday Society* **57**, 1541–1551.

Fripiat, J. J. and della Faille, M. (1967) Surface properties and texture of chrysotiles: *Clays & Clay Minerals* **15**, 305–320.

Hench, L. L. and West, J. K. (1990) The sol-gel process: *Chem. Rev.* **90**, 33–72.

Higuti, I. and Iwagami, Y. (1952) Calorimetric evidence for the capillary condensation theory: *J. Phys. Chem.* **56**, 921–927.

Jackson, C. J. and McKenna, G. B. (1992) A reexamination of the freezing and melting of solvent in thermoreversible polymer gels and related systems: *ASC Polymer Preprints* **32**, 439–440.

Jallut, C., Lenoir, J., Bardot, C., and Eyraud, C. (1992) Thermoporometry. Modelling and simulation of a mesoporous solid: *J. Membr. Sci.* **68**, 271–282.

Jolicoer, C. and Duchesne, D. (1981) Infrared and thermogravimetric studies of the thermal degradation of chrys-

otile asbestos fibres, evidence for matrix effects: *Can. J. Chem.* **59,** 1521–1526.

Low, P. F., Anderson, D. M., and Hoekstra, P. (1968) Some thermodynamic relationships for soils at or below the freezing point. 1. Freezing point depression and heat capacity: *Water Resources Research* **4(2),** 379–394.

Lowell, S. and Shields, J. E. (1984) *Powder Surface Area and Porosity:* 2nd ed., Chapman and Hall, London, 135 pp.

Luys, M.-J., de Roy, G., Vansant, E. F., and Adams, F. (1982) Characterization of asbestos minerals, structural aspects and infrared spectra: *J. Chem. Soc., Faraday Trans.* **78,** 3561–3571.

Miller, R. D. (1973) The porous phase barrier and crystallization: *Separation Science* **8(5),** 521–535.

Noll, W. and Kircher, H. (1951) Über die morphologie von asbesten und ihren zusammenhang mit der kristallstructur: *Neues Jahrbuch für Mineralogie, Monatshefte,* H. O'Daniel, K. H. Scheumann, and H. Schneiderhöhn, eds., 219–240.

Noll, W., Kircher, H., and Sybertz, W. (1958) Adsorptionsvermögen und spezifische Oberfläche von Silikaten mit röhrenförmig gebauten Primärkristallen: *Kolloid Zeitschrift* **157,** 1–11.

Plooster, M. N. and Gitlin, S. N. (1971) Phase transitions in water adsorbed on silica surfaces: *J. Phys. Chem.* **75,** 3322–3326.

Quinson, J. F., Astier, M., and Brun, M. (1987) Determination of surface areas by thermoporometry: *Appl. Catal.* **30,** 123–130.

Sakomoto, T., Nakamura, H., Uedaira, H., and Wada, A. (1989) High-frequency dielectric relaxation of water bound to hydrophylic silica gels: *J. Phys. Chem.* **93,** 357–366.

Sasthav, M., Raj, W. R. P., and Cheung, H. M. (1992) Characterization of microporous polymeric materials. Pore continuity and size distribution via thermal analysis: *J. Coll. Interf. Sci.* **152(2),** 376–385.

Scherer, G. W. (1993) Freezing gels: *J. Non-Crystal. Sol.* **155,** 1–25.

Scholten, J. J. F., Beers, A. M., and Kiel, A. M. (1975) Studies on pore structure of adsorbents and Catalysts: *J. of Catal.* **36,** 23–29.

Suquet, H. (1989) Effects of dry grinding and leaching on the crystal structure of chrysotile: *Clays & Clay Minerals* **37,** 439–445.

Takagi, S. (1990) Approximate thermodynamics of the liquid-like layer on an ice sphere based on an interpretation of the wetting parameter: *J. Coll. Interf. Sci.* **137,** 446–455.

Tasaka, M., Suzuki, S., Ogawa, Y., and Kamaya, M. (1988) Freezing and nonfreezing water in charged membranes: *J. of Membran. Sci.* **38,** 175–183.

Titulaer, M. K. (1993) Porous structure and particle size of silica and hydrotalcite catalyst precursors: Thesis, Rijksuniversiteit Utrecht, *Geologica Ultraiectina* **99,** 268 pp.

Van der Grift, C. J. G., Boon, A. Q. M., Veldhuisen van, A. J. W., Trommar, H. G. J., Geus, J. W., Quinson, J. F., and Brun, M. (1990) Preparation and characterization of porous silica spheres containing a copper(oxide) catalyst: *Applied Catalysis* **65,** 225–239.

Wicks, F. J. and O'Hanley, D. S. (1988) Serpentine minerals, structure and petrology: in *Reviews in Mineralogy: Hydrous Phyllosilicates (Exclusive of Micas)* **19,** S. W. Bailey, ed., BookCrafters, Chelsea and Michigan, 91–129.

Yariv, S. and Heller-Kallai, L. (1975) The relationship between the I.R. spectra of serpentines and their structures: *Clays & Clay Minerals* **23,** 145–152.

Yazynina, I. V., Kvlividze, V. I., and Krasnushkin, A. V. (1987) Thickness of the nondissolving layer of water on a hydrophylic surface: *Coll. J. USSR* **49,** 1188–1194.

Young, G. J. and Healy, F. H. (1954) The physical structure of asbestos: *J. Phys. Chem.* **58,** 881–886.

Zussman, J., Brindley, G. W., and Comer, J. J. (1957) Electron diffraction studies of serpentine minerals: *Amer. Mineral.* **42,** 133–153.